

**Climatology, seasonality and trends of oceanic coherent
eddies**

Josué Martínez-Moreno¹, Andrew McC. Hogg¹, and Matthew H. England²

⁴ Research School of Earth Science and ARC Center of Excellence for Climate Extremes, Australian
⁵ National University, Canberra, Australia

⁶ Climate Change Research Centre (CCRC), UNSW Australia, Sydney NSW, Australia

Key Points:

- ⁸ Kinetic energy of coherent eddies contain around 50% of the surface ocean kinetic
⁹ energy budget.
- ¹⁰ Seasonal cycle of the number of coherent eddies and coherent eddy amplitude re-
¹¹ veal a 3-6 month lag to wind forcing
- ¹² Inverse cascade sets up the seasonal lag of the number and amplitude of coher-
¹³ ent eddies.
- ¹⁴ The coherent eddy amplitude has increase at a rate of 3 cm per decade since 1993.

Corresponding author: Josué Martínez-Moreno, josue.martinezmoreno@anu.edu.au

15 **Abstract**

Ocean eddies influence regional and global climate through mixing and transport of heat and properties. One of the most recognizable and ubiquitous feature of oceanic eddies are vortices with spatial scales of tens to hundreds of kilometers, frequently referred as “mesoscale eddies” or “coherent eddies”. Coherent eddies are known to transport properties across the ocean and to locally affect near-surface wind, cloud properties and rainfall patterns. Although coherent eddies are ubiquitous, yet their climatology, seasonality and long-term temporal evolution remains poorly understood. Thus, we examine the kinetic energy contained by coherent eddies and we present the annual and long-term changes of automatically identified coherent eddies from satellite observations from 1993 to 2019. Around 50% of the kinetic energy contained by ocean eddies corresponds to coherent eddies. Additionally, a strong hemispherical seasonal cycle is observed, with a 3–6 months lag between the wind forcing and the response of the coherent eddy field. Furthermore, the seasonality of the number of coherent eddies and their amplitude reveals that the number of coherent eddies responds faster to the forcing (~ 3 months), than the coherent eddy amplitude (which is lagged by ~ 6 months). Our analysis highlights the relative importance of the coherent eddy field in the ocean kinetic energy budget, implies a strong response of the eddy number and eddy amplitude to forcing at different time-scales, and showcases the seasonality, and multidecadal trends of coherent eddy properties.

35 **Plain language summary**36 **1 Introduction**

Mesoscale ocean variability with spatial scales of tens to hundreds of kilometers is comprised of processes such as vortices, waves, and jets (Ferrari & Wunsch, 2009; Fu et al., 2010). These mesoscale processes are highly energetic, and they play a crucial role in the transport of heat, salt, momentum, and other tracers through the ocean (Wunsch & Ferrari, 2004; Wyrtki et al., 1976; Gill et al., 1974). Possibly, the most recognizable and abundant process observed from satellites is mesoscale vortices. Although mesoscale vortices are commonly referred to in literature as “mesoscale eddies”, this term is also often used to describe the total mesoscale ocean variability (the time-varying component of the mesoscale flow), thus, here we will refer to mesoscale vortices as *coherent eddies*.

46 Coherent eddies are quasi-circular currents. According to their rotational direction,
47 the sea surface height anomaly within a coherent eddy can have a negative or positive
48 sea surface height anomaly (cold-core and warm-core coherent eddies, respectively). This
49 characteristic sea surface height signature of coherent eddies has been utilized to auto-
50 matically identify and track coherent eddies from satellite altimetry (Cui et al., 2020;
51 Martínez-Moreno et al., 2019; Ashkezari et al., 2016; Faghmous et al., 2015; Chelton et
52 al., 2007). Automated identification algorithms of coherent eddies have shown their ubiq-
53 uituity in the oceans, with a predominant influence at hotspots of eddy activity such as bound-
54 ary extensions and the Antarctic Circumpolar Current. In these regions, Chelton et al.
55 (2011) estimated that coherent eddies contribute around 40–50% of the mesoscale kinetic
56 energy (Chelton et al., 2011) and thus a significant fraction of the total kinetic energy
57 (Ferrari & Wunsch, 2009). Although this unique estimate showcases the importance of
58 the mesoscale coherent eddy field, the energy contained by coherent eddies was estimated
59 by extracting the geostrophic velocities within the detected coherent eddies, thus it is
60 possible it may contain energy from other processes. Coherent eddies are not only abun-
61 dant and may have a large proportion of the surface kinetic energy budget, but they are
62 also essential to ocean dynamics as concluded by many previous studies (Patel et al., 2020;
63 Schubert et al., 2019; Pilo et al., 2015; Frenger et al., 2015, 2013; Beron-Vera et al., 2013;
64 Siegel et al., 2011; Hogg & Blundell, 2006).

65 There is broad consensus that mesoscale eddy kinetic energy has a pronounced sea-
66 sonal variability (Uchida et al., 2017; Kang & Curchitser, 2017; Qiu & Chen, 2004; Qiu,
67 1999). Several hypotheses have been proposed to explain this seasonality including: sea-
68 sonal variations of atmospheric forcing (Sasaki et al., 2014), seasonality of the mixed layer
69 depth (Qiu et al., 2014; Callies et al., 2015), seasonality of the intensity of barotropic in-
70 stability (Qiu & Chen, 2004), the variability of the baroclinic instability due to the sea-
71 sonality of the vertical shear (Qiu, 1999), and a seasonal lag of the inverse energy cas-
72 cade (i.e. energy is transported between scales, from small to large; Arbic et al., 2013)
73 in combination with the presence of a front in the mixed layer, which can lead to a sea-
74 sonal cycle of the baroclinic instability (Qiu et al., 2014). On one hand, processes such
75 as barotropic and baroclinic instabilities control the seasonality of coherent eddies in the
76 ocean. On the other hand, recent studies using observations and eddy-permitting climate
77 models suggest several long-term adjustments of the global ocean capable of long-term
78 changes in the coherent eddy field. Such readjustments include a multidecadal increase

in the ocean stratification resulted from temperature and salinity changes (Li et al., 2020), a horizontal readjustment of the sea surface temperature gradients (Ruela et al., 2020; Bouali et al., 2017; Cane et al., 1997), and an intensification of the kinetic energy, eddy kinetic energy, and mesoscale eddy kinetic energy over the last 3 decades as a consequence of an increase in wind forcing (Hu et al., 2020; Wunsch, 2020; Martínez-Moreno et al., 2021). All these seasonal factors and long-term readjustments directly influence the annual and decadal response of the coherent eddy field, however, the seasonality of the coherent component of the eddy kinetic energy, as well as the seasonal cycle and trends of the coherent eddy statistics remain unknown.

Here we present a new global climatology of the coherent eddy kinetic energy by reconstructing the coherent eddy signature from satellite observations. Our study documents the seasonal cycle of the coherent eddy kinetic energy, and seasonal cycle and long-term trends of the coherent eddy properties over the satellite record. Moreover, we conduct more detail analysis in regions where coherent eddies dominate the eddy kinetic energy field. This paper is structured as follows: the data sources and methodology are described in section 2. Then, we present the climatology, energy ratios, and global seasonality of the coherent eddy kinetic energy in section 3. Section 4 presents the global climatology and seasonality of coherent eddy properties, followed by long-term changes of the coherent eddy properties (section 5). Then we focus our attention on the seasonal cycle and coherent eddy properties in regions dominated by coherent eddies (section 6). Finally, section 7 summarizes the main results and discusses the implications of this study.

2 Methods

We use daily sea surface height (SSH) data made available by the Copernicus Marine Environment Monitoring Service in near real time (CMEMS, 2017). This gridded product contains the sea surface height and geostrophic velocities with daily 0.25° resolution from January 1993 to 2019. The daily geostrophic velocities allowed us to compute the kinetic energy (KE) and eddy kinetic energy (EKE) over the satellite record. The main source of EKE is the time-varying wind (Ferrari & Wunsch, 2009), thus we computed the seasonal cycle of the wind magnitude from the JRA55 reanalysis (Japan Meteorological Agency, Japan, 2013) using wind velocities at 10m above the ocean's surface.

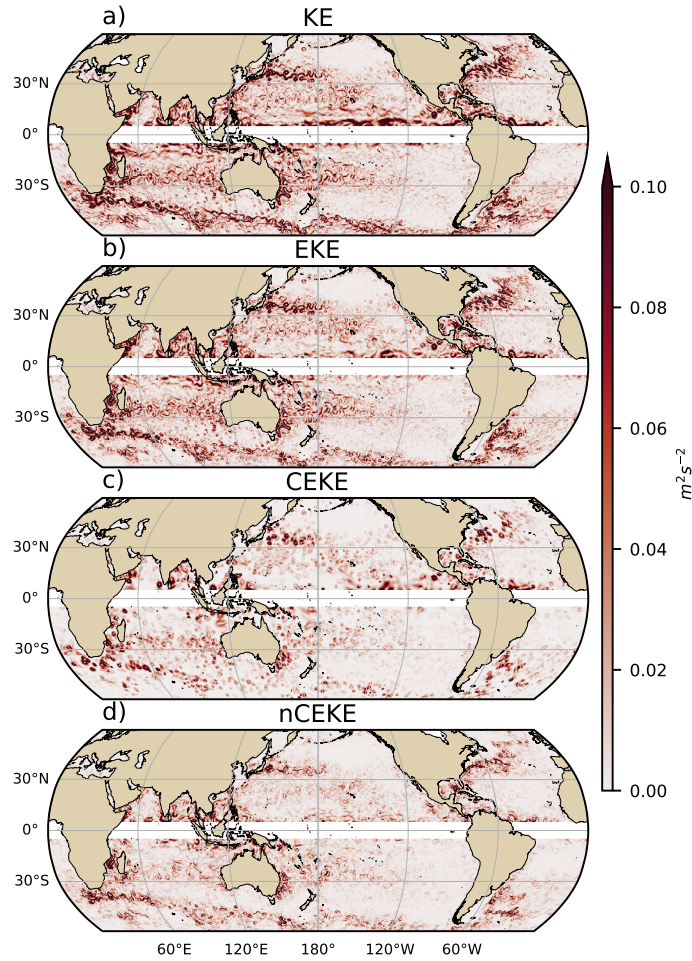
Over the same record, coherent eddy statistics from Martínez-Moreno et al. (2019), hereafter M-M, are analyzed and compared to those released by Chelton & Schlax (2013), both datasets are gridded in a 1° resolution. Although both datasets are produced via automated eddy identification algorithms using closed contours of SSH, these datasets have important differences in the criteria they use to identify and record coherent eddies statistics. The major differences include; (i) M-M's algorithm requires an adjustment between a 2D Gaussian and the SSH anomaly (SSHa) surface within the identify closed contour, while Chelton's only uses the outer-most closed contour of SSH; (ii) M-M's dataset reports the maximum SSHa within the identified coherent eddy, while Chelton's algorithm reports the maximum SSH value minus the discrete level in which the coherent eddy was identified; M-M's dataset includes all detected coherent eddies, while Chelton's dataset excludes (iii) coherent eddies with lifetimes shorter than four weeks and (iv) coherent eddy amplitudes smaller than 1cm. Moreover, M-M's algorithm allows the reconstruction of the coherent eddy field under the assumption that coherent eddies have a 2D Gaussian imprint in the sea surface height. This Gaussian reconstruction of the coherent eddy field then allow us to estimate the coherent geostrophic eddy velocities and thus the kinetic energy contained only by coherent eddies.

2.1 Kinetic Energy decomposition

Kinetic energy is commonly divided into the mean and time-varying components through a Reynolds decomposition. At a given time, the surface velocity field $\mathbf{u} = (u, v)$ is split into the time mean ($\bar{\mathbf{u}}$) and time varying components (\mathbf{u}'). Moreover, M-M proposed to further decompose the eddy kinetic energy into the energy contained by coherent features (\mathbf{u}'_e) and non-coherent features (\mathbf{u}'_n). Therefore the KE equation can be written as:

$$\text{KE} = \underbrace{\bar{u}^2 + \bar{v}^2}_{\text{MKE}} + \underbrace{u'^2_e + v'^2_e + u'^2_n + v'^2_n}_{\text{CEKE}} + \underbrace{\mathcal{O}_c^2}_{\text{nCEKE}} + \mathcal{O}^2 \quad (1)$$

Due to the properties of this decomposition, the second order term \mathcal{O}^2 is zero when averaged over the same period as $\bar{\mathbf{u}}$. However, \mathcal{O}_c^2 is not necessarily negligible, unless it is averaged over time and space. More information about the decomposition of the field into coherent features and non-coherent features is explained by Martínez-Moreno et al.



143 **Figure 1.** Snapshot of surface kinetic energy (\overline{KE}), surface eddy kinetic energy (\overline{EKE}),
 144 surface coherent eddy kinetic energy (\overline{CEKE}), and surface non-coherent eddy kinetic energy
 145 (\overline{nCEKE}) for the 1st of January 2017.

138 (2019). A global snapshot of each component of kinetic energy decomposition is shown
 139 in Figure 1, where the KE and EKE are comprised of rings and filaments. As expected,
 140 the decomposition of EKE into CEKE and nCEKE components exhibit only ring-like
 141 signatures expected of coherent eddies, while the non-coherent component shows filaments
 142 and some miss-identified coherent eddies.

146 2.2 Eddy statistics

147 The eddy statistics used in this study include (i) the eddy count ($cEddy_n$) defined
 148 as the number of eddies per grid cell, (ii) the eddy diameter defined as the diameter of

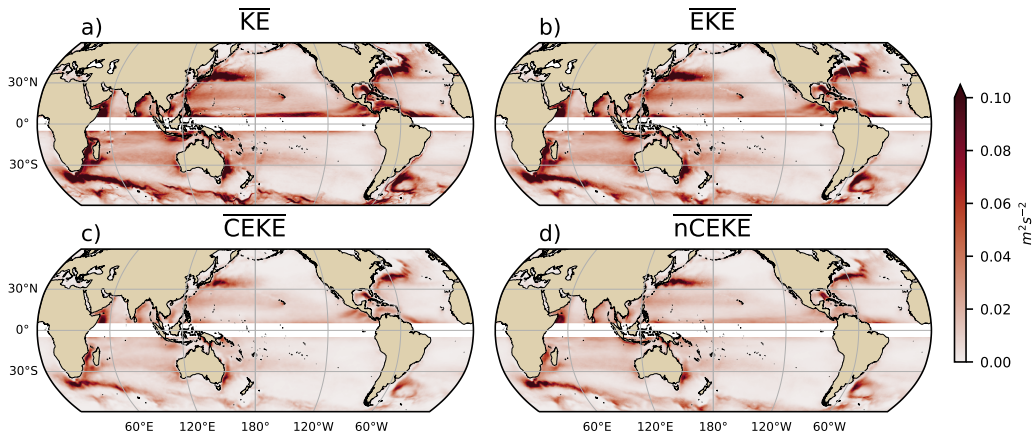
a circle with equal area as the closed contour of the identified eddy, and (iii) the mean eddy amplitude defined as the mean amplitude of the coherent eddies within the cell ($cEddy_{amp}$). The latter metric can be separated into positive ($cEddy_{amp}^+$) and negative ($cEddy_{amp}^-$) coherent eddy amplitudes, defined as the mean amplitude of warm core and cold core coherent eddies, respectively, within the cell. The absolute eddy amplitude ($|cEddy_{amp}|$) is then defined as:

$$|cEddy_{amp}| = \frac{1}{2} (cEddy_{amp}^+ - cEddy_{amp}^-) \quad (2)$$

Note that the $cEddy_{amp}^+$ and $cEddy_{amp}^-$ are sign definite, thus the difference will always be positive, mean $cEddy_{amp}$ can be negative or positive noting the dominant polarity of coherent eddies in the region. We analyze the climatology, seasonal cycles and trends of the eddy statistics between 1993 and 2019. We exclude the equatorial region (10°S - 10°N) and poleward of 60° . Note that the climatology of $cEddy_n$ is computed by adding all the identified eddies over the record, while all other climatological statistics are computed as the time-average over the record. Seasonal climatologies are calculated for the monthly average of each coherent eddy statistic, while hemispherical time-series are filtered with a running average of 90 days. Trends of $cEddy_n$ and $|cEddy_{amp}|$ are calculated by coarsening the dataset to a 5° grid, and then linear trends are computed for each grid point, the statistical significance is assessed by a modified Mann-Kendall test (Yue & Wang, 2004). Time averages are denoted by $\overline{}$, while time and area averages are shown by $\langle \rangle$.

3 Global Coherent Eddy Energetics

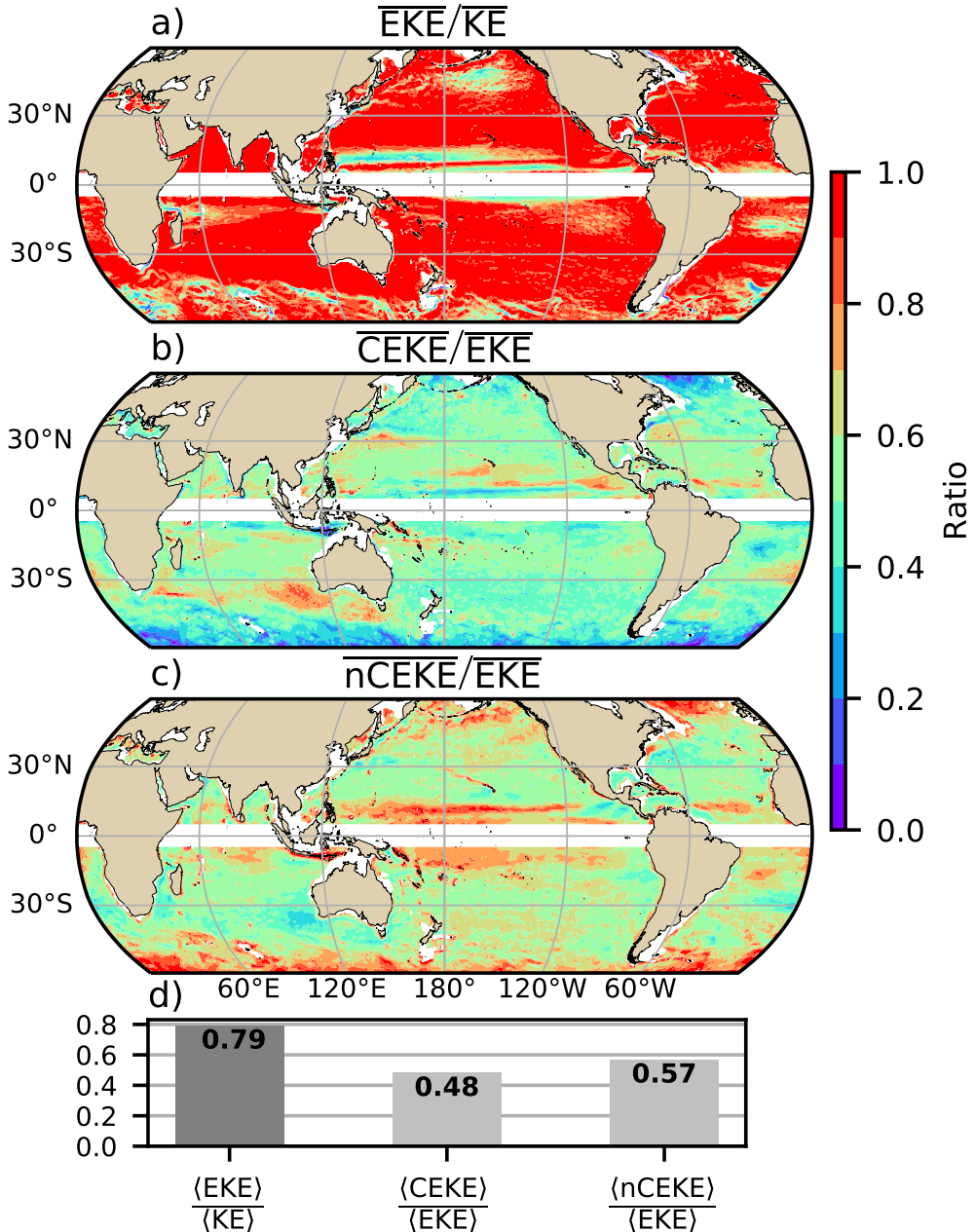
The kinetic energy decomposition estimated from sea surface height measured by satellite altimeters is shown in Figure 2. These maps show that many regions of the global ocean are highly energetic in mean KE (\overline{KE}), mean EKE (\overline{EKE}), mean coherent eddy kinetic energy (\overline{CEKE}) and mean non-coherent eddy kinetic energy (\overline{nCEKE}). The spatial pattern highlights well known regions of the ocean where mesoscale processes are abundant, such as the western boundary extensions and the Antarctic Circumpolar Current. Remarkably, the spatial distribution of the energy contained by the reconstructed mesoscale coherent eddies and non-coherent components are similar (Figures 2c,d). However, there are some regions where coherent eddies dominate over non-coherent, and vice-versa. Overall, this decomposition suggest that boundary current extensions and other energetic re-



181 **Figure 2.** Mean surface kinetic energy (\overline{KE}), surface eddy kinetic energy (\overline{EKE}), surface
182 coherent eddy kinetic energy (\overline{CEKE}), and surface non-coherent eddy kinetic energy (\overline{nCEKE})
183 between 1993–2018.

179 gions, in particular, eddy-rich regions in the ocean contain both coherent and non-coherent
180 components of the kinetic energy.

193 Eddy kinetic energy is known to be more than an order of magnitude greater than
194 MKE (Gill et al., 1974); this result is clearly shown in Figure 3a, where \overline{EKE} is respon-
195 sible for almost all the \overline{KE} across the ocean, except for regions with persistent currents
196 over time. Such regions are located in the mean boundary extension locations, the equa-
197 torial Pacific currents and regions in the Antarctic Circumpolar Current, where the \overline{EKE}
198 explains around 40% of the \overline{KE} . In a previous study, Chelton et al. (2011) estimated that
199 the EKE within coherent eddies with lifetimes greater than 4 weeks contain between 40
200 to 60 percent of the \overline{EKE} . Our method to reconstruct the coherent eddy signature (Fig-
201 ure 3b) further corroborates that the coherent component (\overline{CEKE}) has \sim 48% of the \overline{KE}
202 (Figure 3d). Furthermore, global area averages of the ratios show \overline{EKE} explains \sim 78%
203 of the ocean \overline{KE} field, while non coherent eddy features contain \sim 57% percent of the \overline{EKE} .
204 Note the globally averaged coherent and non coherent components do not add to 100%
205 as the cross terms (\mathcal{O}_c^2) are non-zero, as regions with **weak** EKE are double counted in
206 the CEKE and nCEKE ratios, and coherent eddy reconstruction errors. The spatial pat-
207 tern reveals a dominance of the \overline{CEKE} equatorward from the boundary extensions and
208 areas with large coherent eddy contributions of around 80% of the region's eddy kinetic
209 energy can be found south of Australia, the Tehuantepec Gulf, and the tropical Atlantic.



184 **Figure 3.** Ratios of the kinetic energy components. a) Map of the proportion of mean eddy
 185 kinetic energy (\overline{EKE}) versus mean kinetic energy (\overline{KE}); b) Map of the percentage of mean co-
 186 herent eddy kinetic energy (\overline{CEKE}) versus mean eddy kinetic energy (\overline{EKE}); c) Map of the
 187 percentage of mean non-coherent eddy kinetic energy (\overline{nCEKE}) versus mean eddy kinetic energy
 188 (\overline{EKE}); d) Global time and area averaged (represented by $\langle \rangle$) percentage of mean eddy kinetic
 189 energy ($\langle \overline{EKE} \rangle$) versus the global mean kinetic energy ($\langle \overline{KE} \rangle$), area averaged percentage of mean
 190 coherent eddy kinetic energy ($\langle \overline{CEKE} \rangle$) and mean non coherent eddy kinetic energy ($\langle \overline{nCEKE} \rangle$)
 191 versus global mean eddy kinetic energy ($\langle \overline{EKE} \rangle$). Regions where the depth of the ocean is shall-
 192 lower than 1000m are removed from the ratio estimation.

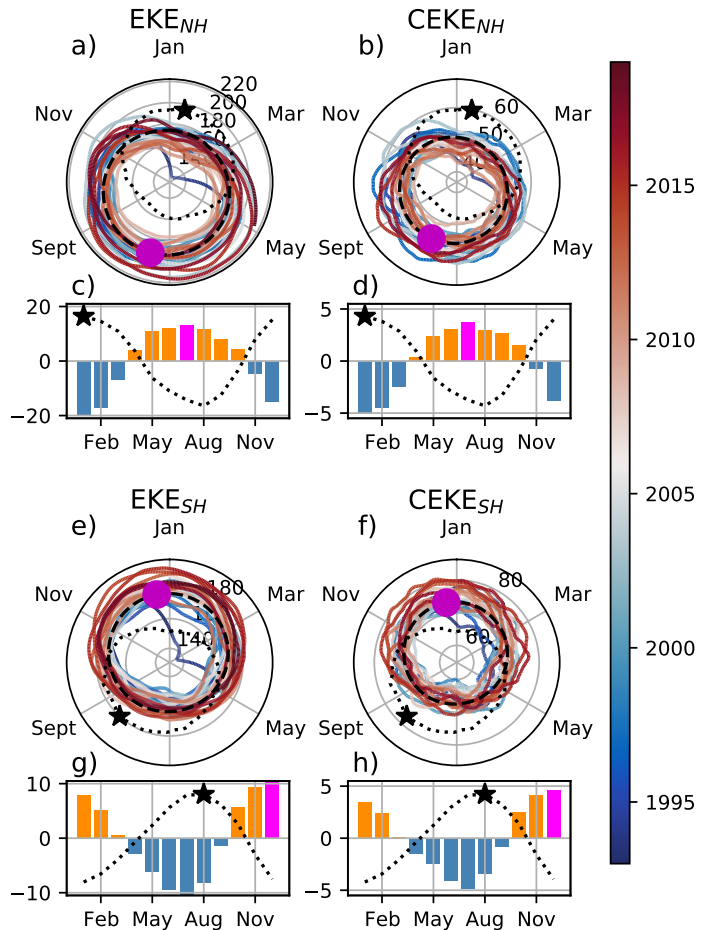
210 An evident signal is an reduction of the energy contained by coherent eddies at high latitudes
 211 and an increase in the energy explained by non-coherent eddies; this signal could
 212 be a consequence of the incapability of the 0.25° satellite resolution (~ 13 km at 60°)
 213 to resolve coherent eddies with scales smaller than ~ 10 km (first baroclinic Rossby radius
 214 at 60° ; Chelton et al. 1998).

215 Figure 4 shows the seasonal cycle of the EKE and CEKE for the Northern Hemisphere
 216 (NH; 10°N - 60°N) and Southern Hemisphere (SH; 60°S - 10°S). In both hemispheres,
 217 the EKE and CEKE peak during summer. In the Northern Hemisphere, the largest
 218 EKE and CEKE occurs ~ 6 months after the maximum winds (Figure 4c and d), while
 219 the Southern Ocean seems to respond within ~ 4 months (Figure 4g, and h). This sea-
 220 sonal lag and maximum is consistent with a time-lag of the inverse cascade (Sasaki et
 221 al., 2014; Qiu et al., 2014) where winter has the highest energy at the smallest scales (non-
 222 resolvable with satellite observations), spring and autumn have the highest and lowest
 223 energy in scales of 50-100 km, and summertime has the highest energy at the largest scales
 224 (> 100 km; Uchida et al. 2017). Thus, the maximum of EKE and CEKE located dur-
 225 ing summertime suggest that the seasonality of eddies and coherent eddies could be dom-
 226 inated by scales larger than 100 km.

227 The cyclic plots in Figure 4 show the temporal evolution of EKE and CEKE. Note
 228 that high frequency variability can be observed in the CEKE field with temporal scales
 229 of a few months, this could be attributed local dynamics averaged over the hemisphere,
 230 as well as errors within the coherent eddy reconstruction. Additionally, cyclic plots high-
 231 light long-term temporal changes over the record; (i) Northern Hemisphere winters show
 232 a decrease in the CEKE field and (ii) the Southern Hemisphere show concentric growth
 233 over time in EKE and CEKE, which support the increasing trends in the Southern Ocean
 234 observed by Hogg et al. (2015), Martínez-Moreno et al. (2019), and Martínez-Moreno
 235 et al. (2021).

244 4 Global Coherent Eddy Statistics

245 Automated coherent eddy identification algorithms allow us to estimate the con-
 246 tribution and temporal changes of eddy properties, in particular, their abundance (the
 247 number of eddies) and their intensity (both their amplitude and diameter). Figure 5 shows
 248 gridded climatologies of the number of eddies and the eddy amplitude. We contrast M-



236 **Figure 4.** Seasonality of eddy kinetic energy (EKE), coherent eddy kinetic energy (CEKE).
 237 Panels a and b show the time-series of the Northern Hemisphere, while panels e and f correspond
 238 to the Southern Hemisphere. Panels c and d show the seasonal cycle of the EKE and CEKE in
 239 the Northern Hemisphere, and panels g and h show the Southern Hemisphere. Dashed lines cor-
 240 respond to the seasonal cycle of the fields and dotted lines show the seasonal cycle of the wind
 241 magnitude smoothed over 120 days (moving average). The black and magenta markers (circle
 242 and bar) show the maximum of the seasonal cycle for the kinetic energy components and the
 243 wind magnitude, respectively. In cyclic plots, line colors shows the year.

M eddy count with Chelton et al. (2007) (Figure 5a-b). Although the number of the identified eddies is larger in M-M, possibly due to the lifespan filter implemented by Chelton, both datasets reveal consistent spatial patterns. For example, both datasets show high abundance of eddies in the East North Pacific, East North Atlantic, as well as the East South Pacific, East South Atlantic and East Indian Ocean, and small number counts of eddies in the tropics and in high latitudes ($\sim 60^\circ$). An interesting pattern also emerges in both eddy count datasets, where clusters with larger eddy counts are favored across the ocean. In addition, to preferential coherent eddy paths observable in boundary extensions and regions in the Southern Ocean. These clusters and paths of coherent eddies could be associated with topographic features, however they remain a puzzling consistency between the eddy count pattern using these two eddy identification methods.

Regions with large counts of eddies have in general small absolute amplitudes (Figure 5 c), ocean gyre interiors follow with a larger absolute amplitude and finally regions such as the boundary extensions and Antarctic Circumpolar Current have the largest coherent eddy absolute amplitudes as shown by Chelton et al. (2011). Eddy amplitude highlights regions dominated by a given coherent eddy polarity, for example, boundary extensions have a preferred sign (Figure 5 d); positive amplitude polewards of the boundary extension mean location, and negative amplitude equatorwards. This sign preference is consistent with the way coherent eddies are shed from boundary extensions (Kang & Curchitser, 2013; Chelton et al., 2011, 2007). These global statistics reveal the absolute coherent eddy amplitude is a proxy of the CEKE with similar spatial patterns (Figure 2 & Figure 5 c) and showcases that regions where $\overline{\text{CEKE}}$ has a large proportion of $\overline{\text{EKE}}$ (Figure 3), the absolute coherent eddy amplitude is also large.

To further understand the seasonal cycle of CEKE, we compute the climatology of coherent eddy properties in each hemisphere (Figure 6). The seasonality of the number of eddies in the Northern Hemisphere peaks on April (Figure 6 a, c), while the Southern Hemisphere maximum number of eddies occurs during October (Figure 6 e, g). Meanwhile, the seasonality of the absolute eddy amplitude peaks in August and January for the Northern and Southern Hemispheres respectively (Figure 6 b, d, f, and h). As expected, the seasonality of the absolute eddy amplitude, or intensity of the coherent eddies, is consistent with the seasonal cycle of CEKE. Furthermore, a distinct lag of ~ 3 months is observed between the winds and eddy count, while the eddy amplitude maximum occurs ~ 6 months after the seasonal maxima in winds. This lag suggest the eddy

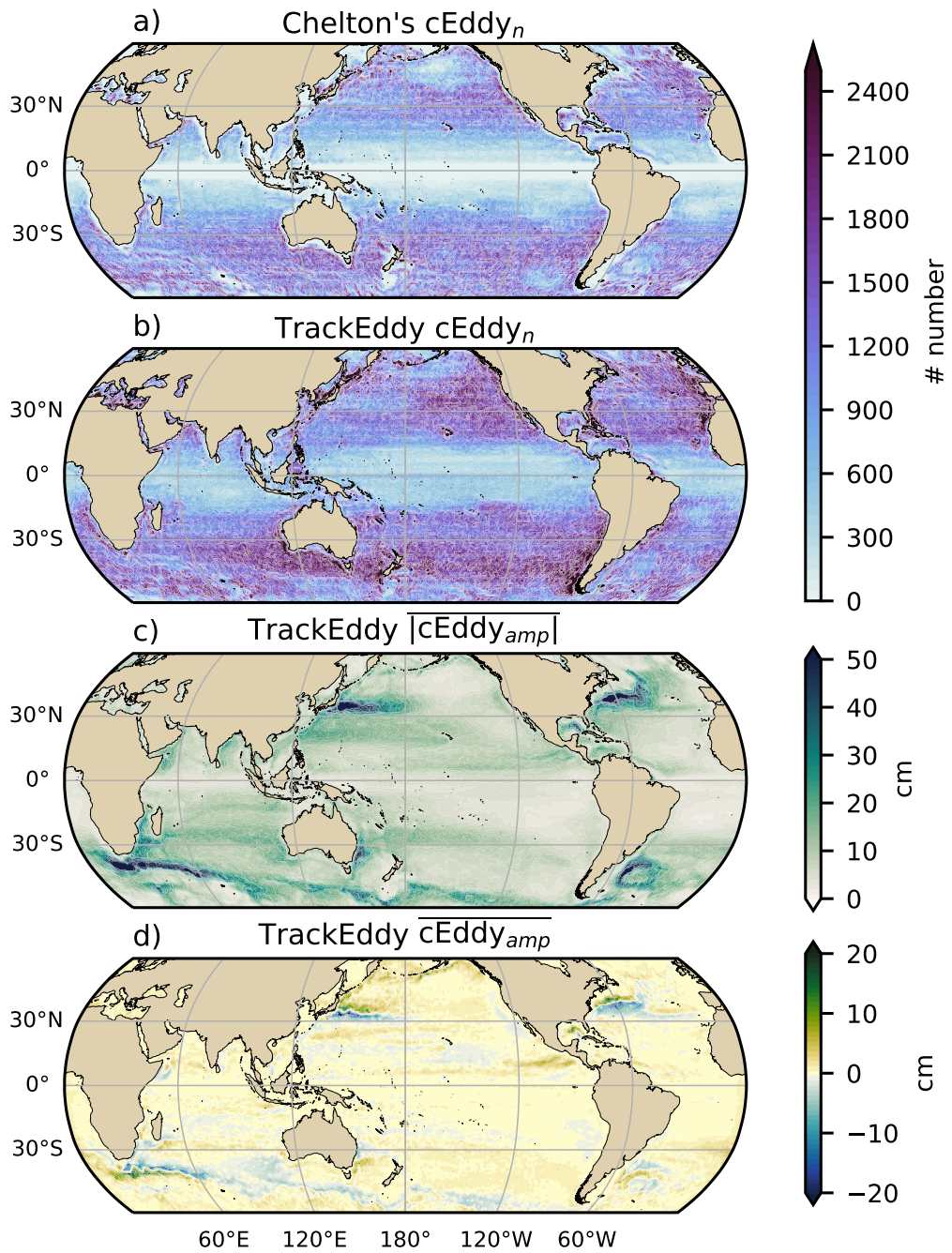


Figure 5. Averaged coherent eddy statistics. a) Climatology of the number of coherent eddies ($cEddy_n$) identified by Chelton et al. (2007); b) Climatology of the number of coherent eddies ($cEddy_n$) identified by Martínez-Moreno et al. (2019); c) Climatology of the mean absolute coherent eddy amplitude ($cEddy_{amp}$). d) Climatology of the mean coherent eddy amplitude ($cEddy_{amp}$).

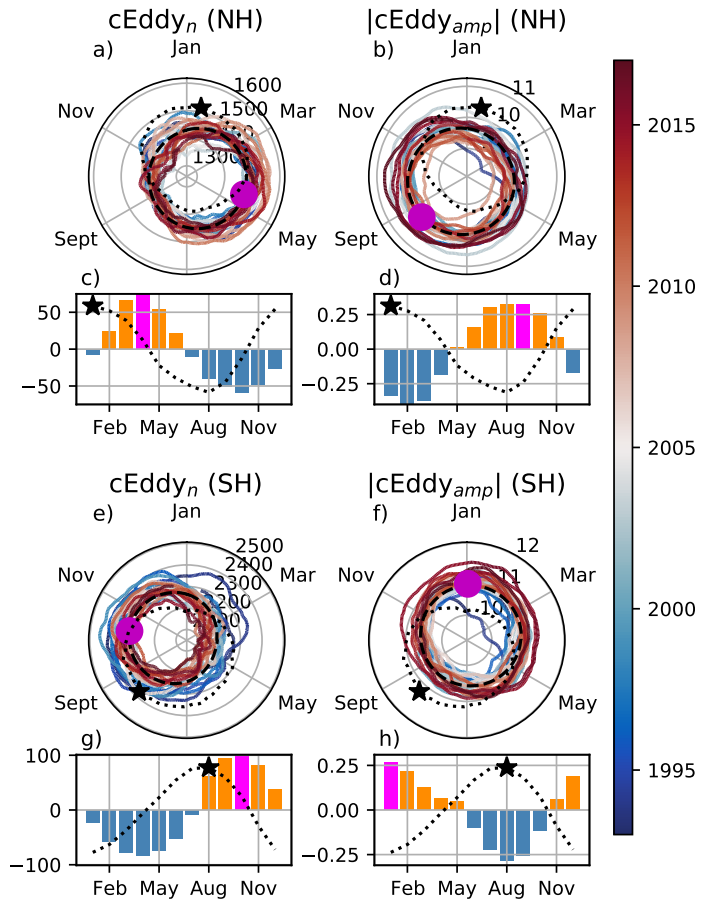
number increases earlier in the year and through eddy-eddy interactions (merging of coherent eddies) the amplitude of the coherent eddy increases. This result can be further explored by looking at the seasonal evolution of the eddy diameter. Note that 90% of identified coherent eddies have diameters between 50 to 220 km (Figure 7 a). We divided eddies into large-scale coherent eddies (diameter > 120 km) and small-scale coherent eddies (diameter < 120 km; Figure 7a). In the Northern Hemisphere, small eddies have a seasonal peak in XXX diameter during May, while large eddies have the greatest diameter in September (Figure 7 b). Meanwhile, in the Southern Hemisphere, the small-scale coherent eddies have the maximum diameter in December, while large-scale coherent eddies peak in February (Figure 7 c). This result suggests that wind driven baroclinic instabilities generate small coherent eddies early in the season, which then merge and grow to become larger in diameter and amplitude, and thus, more energetic. This process is associated with the inverse energy cascade, and suggest that this mechanism not only drives the EKE seasonality, but also may be responsible of the seasonal cycle of coherent eddies.

Long-term changes can be observed in Figure 6a,b, e, and f where growing-shrinking concentric circles over time denote an increase-decrease trend of the field. This trend is particularly evident in the Southern Hemisphere, where the number of eddies has decreased, the eddy amplitude has increased. This result is consistent with the observed trends in EKE and mesoscale EKE in the Southern Ocean (Hogg et al., 2015; Martínez-Moreno et al., 2019).

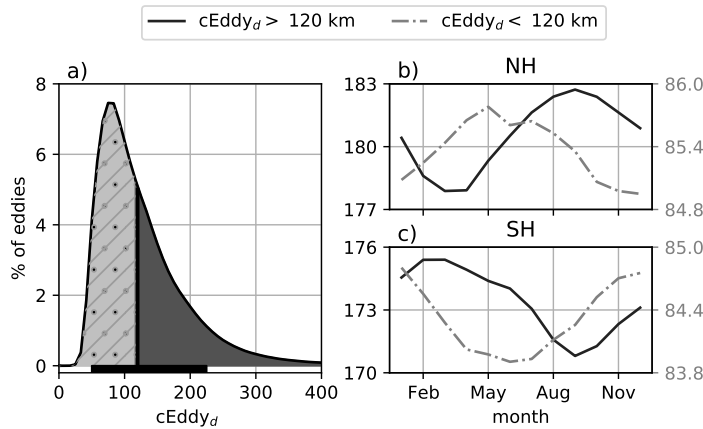
The coherent eddy amplitude from positive coherent eddies and negative coherent eddies show similar seasonal cycles to the absolute eddy amplitude (Figure 8). However, by separating the polarity contribution, its observed that the amplitude of negative coherent eddies in the Northern Hemisphere has decreased (Figure 8b). In the Southern Ocean, the increase in absolute eddy amplitude is further corroborated as both coherent eddy polarities show an increase since the early 90s (Figure 8e,f).

5 Trends

The results presented in Figures 4, 6, and 8 suggest a long-term readjustment of the coherent eddy field. The long-term trends of the number of coherent eddies, absolute coherent eddy amplitude, and coherent eddy amplitude polarities are explored in



308 **Figure 6.** Hemispherical seasonality of the coherent eddy statistics; a,e) seasonal cycle of the
 309 number of coherent eddies ($cEddy_n$); b,f) seasonal cycle of the mean coherent eddy amplitude
 310 ($cEddy_{amp}$); c,g) seasonal cycle of the warm core coherent eddies amplitude (positive $cEddy_{amp}$);
 311 d,h) seasonal cycle of the cold core coherent eddies amplitude (negative $cEddy_{amp}$). Panels a,b
 312 and c show the Northern Hemisphere seasonal cycle, while panels d,e, and f correspond to the
 313 Southern Hemisphere. Dashed lines correspond to the seasonal cycle of the fields and dotted lines
 314 show the seasonal cycle of the wind magnitude smoothed over 120 days (moving average). The
 315 green and magenta stars show the maximum of the seasonal cycle for each field and the wind
 316 magnitude, respectively. The line colors show the year.

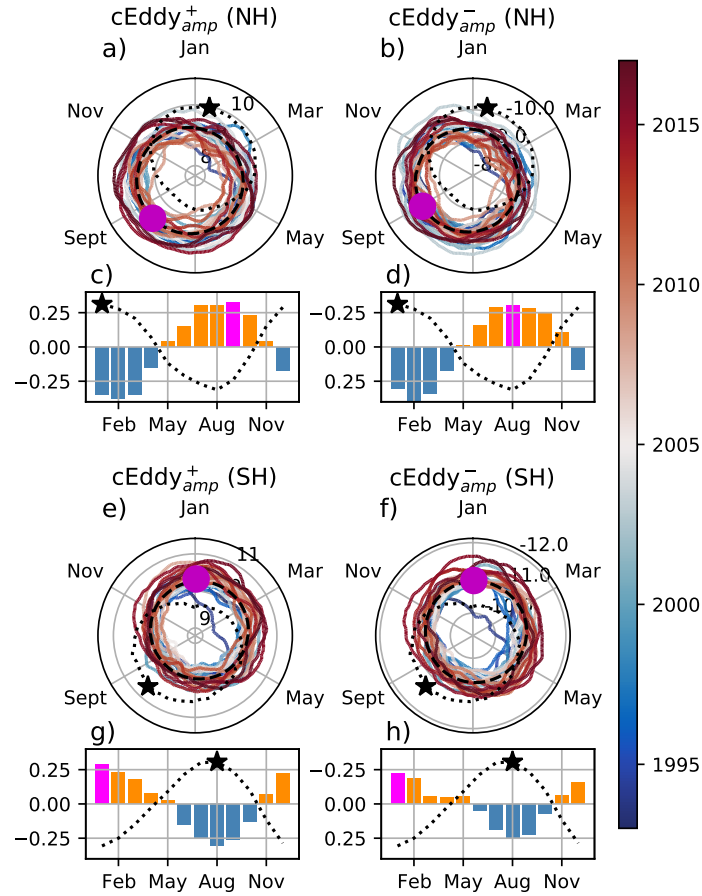


317 **Figure 7.** Distribution of the identified eddy diameter ($cEddy_d$; km) and hemispherical
 318 seasonality of the coherent eddy diameter. a) Distribution in percentage of identified eddy am-
 319 plitude, solid bar below distribution represents 90% of the identified eddies. Seasonal cycle of
 320 the eddy diameter for the b) Northern Hemisphere and c) Southern Hemisphere. Dark solid line
 321 and area corresponds to coherent eddies with diameters larger than 120 km, while light gray
 322 dash-dotted line and area shows coherent eddies with diameters smaller than 120 km.

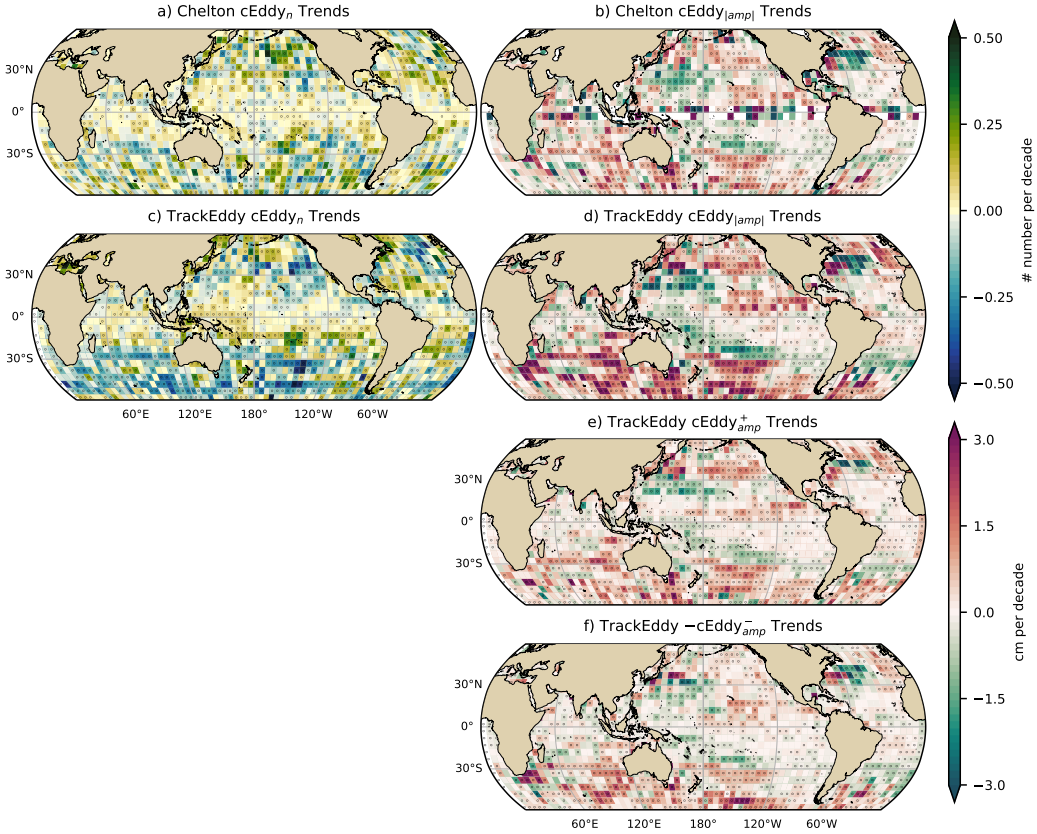
342 Figure 9. Chelton's and M-M datasets show consistent spatial patterns in the trends and
 343 significance of the number of coherent eddies and the absolute coherent eddy amplitude.
 344 Several regions in the ocean, such as the Southern Ocean, North Atlantic and North Pa-
 345 cific, show a decrease in the number of eddies. Those same regions also have a clear in-
 346 crease in the absolute coherent eddy amplitude. These trends are similar to those ob-
 347 served in mesoscale eddy kinetic energy (Martínez-Moreno et al., 2021) and provide ad-
 348 dditional evidence of a readjustment of the mesoscale eddy field over the last 3 decades.

349 in several regions in the ocean are experiencing

350 The observed trends of $|cEddy_{amp}|$ in several oceanic regions have the same scale
 351 as sea level rise ($\sim 3\text{cm}$ per decade) by analyzing the positive and negative coherent eddy
 352 amplitude we can discard the observed trends correspond to an increase in sea level. In
 353 fact, each coherent eddy polarity has intensified in the Southern Ocean and North East
 354 Pacific and Atlantic. In other words, the absolute amplitude of each polarity has increased
 355 over time, thus this strengthening is an intrinsic response of the coherent eddy field. Note
 356 that the negative coherent eddy amplitude dominates the global $|cEddy_{amp}|$ trends (Fig-
 357 ure 9e, f). However, different trend pattern can be observed in both positive and neg-



329 **Figure 8.** Hemispherical seasonality of the coherent eddy statistics; a,e) seasonal cycle of
 330 the number of coherent eddies ($cEddy_n$); b,f) time-series of the mean coherent eddy amplitude
 331 ($cEddy_{amp}$); c,g) seasonal climatology of the warm core coherent eddies amplitude (positive
 332 $cEddy_{amp}$); d,h) seasonal climatology of the cold core coherent eddies amplitude (negative
 333 $cEddy_{amp}$). Panels a, b, c, and d correspond to the Northern Hemisphere, while panels e, f, g,
 334 and h correspond to the Southern Hemisphere. Dashed lines correspond to the seasonal cycle of
 335 the fields and dotted lines show the seasonal cycle of the wind magnitude smoothed over 120 days
 336 (moving average). The green and magenta stars show the maximum of the seasonal cycle for each
 337 field and the wind magnitude, respectively. The line colors show the year.



361 **Figure 9.** Trends of coherent eddy statistics. a) and b) Trends of the number of identified
 362 coherent eddies from satellite observations identified using TrackEddy, and those reported in
 363 Chelton's dataset. c) and d) Trends of the mean absolute value of identified coherent eddies am-
 364 plitude from satellite observations identified using TrackEddy, and those reported in Chelton's
 365 dataset. e) and f) Trends of eddy amplitude polarity using TrackEddy. Gray stippling shows
 366 regions that are statistically significant above the 95% confidence level. **Change $cEddy_{amp}$ to**
 367 **$|cEddy_{amp}|$**

358 ative coherent eddy amplitudes in the north Atlantic and north Pacific, where the neg-
 359 ative coherent eddy amplitude in the Western Boundary Currents appears to decrease
 360 and is consistent with Figure 8.

368 6 Regional Climatology

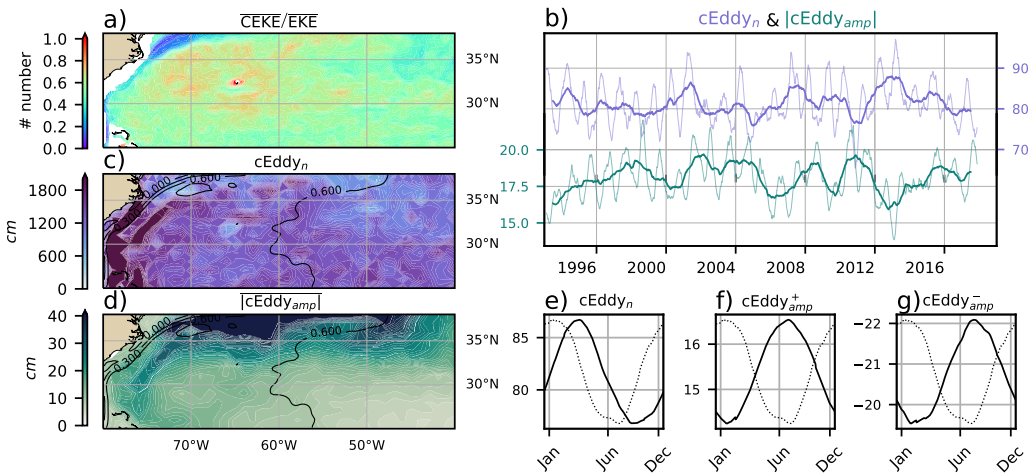
369 For regions with relatively large proportions of CEKE located at boundary exten-
 370 sions and eastern currents, we investigate the seasonal and long-term variability of the
 371 coherent eddy properties.

372 The most energetic western boundary extensions include; the Gulf Stream, the Kuroshio
 373 Current, and the Agulhas Current (Figures 10, 11, and 12). Coherent eddy generation
 374 in boundary extensions occurs through baroclinic and barotropic instabilities of the mean
 375 current, thus all these regions share similar generation dynamics. In all these regions with-
 376 out exception; (i) CEKE contains up to 80% of the EKE in regions equatorwards from
 377 the mean western boundary extension location, (ii) the number of eddies is consistently
 378 minimal numbers of eddies over the mean western boundary extension location, and (iii)
 379 the absolute eddy amplitude is larger polewards of the mean western boundary exten-
 380 sion location.

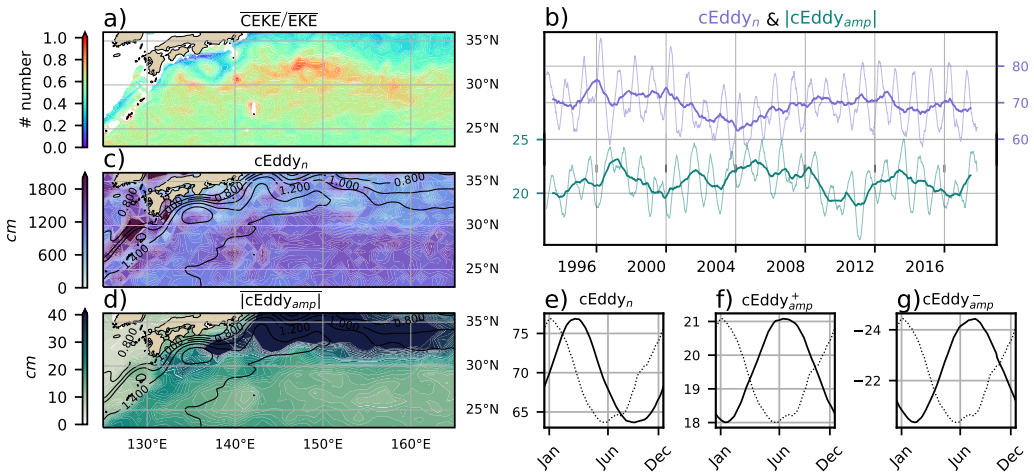
381 In the Gulf Stream, the energy ratio between CEKE and EKE is \sim 55% (Figure 10).
 382 The highest energy content occurs in regions with numerous eddies, and collocated with
 383 regions where the largest $|cEddy_{amp}|$ gradients occurs. The time series of $cEddy_n$ and
 384 $|cEddy_{amp}|$ are anti-correlated (-0.52), and they display inter-annual and seasonal vari-
 385 ability. Although Chaudhuri et al. (2009) observed a positive phase of North Atlantic
 386 Oscillation (NAO) exhibit higher EKE, due to an increase in baroclinic instabilities, thus
 387 suggesting more coherent eddies, we do not find a correlation between the $cEddy_n$ or the
 388 $|cEddy_{amp}|$ in the Gulf Stream and the NAO index. Similar to the signal observed in
 389 the hemispherical analysis, the eddy count seasonal cycle follows the wind maximum af-
 390 ter \sim 3 months, while the amplitude of the coherent eddies lags by \sim 6 months.

399 The variability of the $cEddy_n$ and $|cEddy_{amp}|$ in the Kuroshio Current are weakly
 400 anti-correlated (-0.4; Figure 11). However, on average 56% of the energy in the region
 401 corresponds to CEKE. As observed in the Gulf Stream, there is an important seasonal
 402 cycle in the boundary extensions, where the eddy count seasonal cycle occurs on March
 403 after \sim 3 months of the wind maximum (January). Meanwhile, the amplitude of the co-
 404 herent eddies lags by \sim 6 months (June) after the maximum wind.

411 In the Southern Hemisphere, the strongest boundary current, the Agulhas Current
 412 shows similar behavior to its counterparts in the Northern Hemisphere (Figure 12). On
 413 average, coherent eddies in the Agulhas current contain \sim 56% of the energy, meanwhile
 414 the $cEddy_n$ seasonal peak occurs in August, while the $|cEddy_{amp}|$ occurs in January-
 415 February. The seasonal lag between the winds, eddy count, and eddy amplitude in each
 416 of the western boundary current extensions is interpreted as being analogous to the ex-



391 **Figure 10.** Climatology of the eddy field and coherent eddy field at the Gulf Stream. a) Ratio
 392 of mean coherent eddy kinetic energy ($\overline{\text{CEKE}}$) versus mean eddy kinetic energy ($\overline{\text{EKE}}$); b) Thick
 393 lines show the running average over 2 years and thin lines show the running average over 90 days
 394 of the coherent eddy number sum and the average absolute coherent eddy amplitude; c) Map of
 395 the number of eddies; d) Map of the average absolute coherent eddy amplitude; e) Seasonal cycle
 396 of the number of eddies f) Seasonal cycle of the positive coherent eddy amplitude. g) Seasonal
 397 cycle of the negative coherent eddy amplitude. Contours in maps correspond to mean sea surface
 398 height (m).

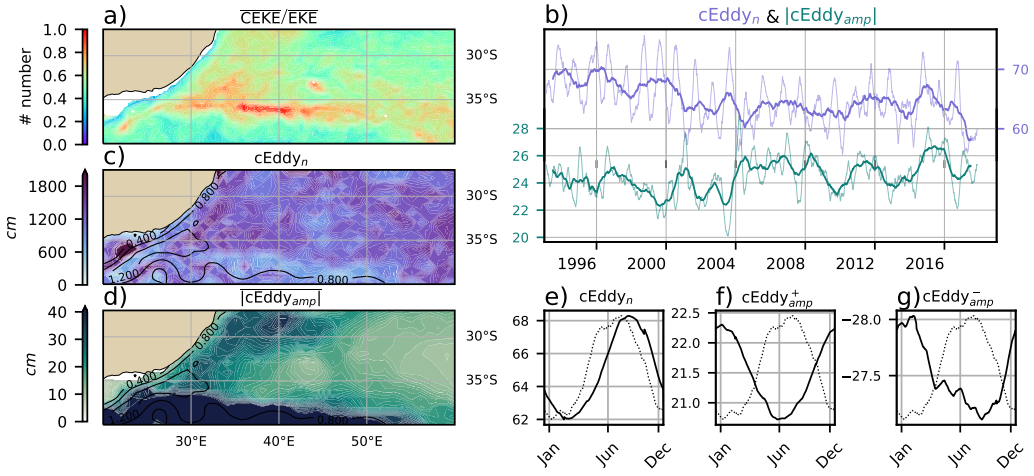


405 **Figure 11.** Climatology of the eddy field and coherent eddy field at the Kuroshio extension.
 406 a) Ratio of mean coherent eddy kinetic energy ($\overline{\text{CEKE}}/\overline{\text{EKE}}$) versus mean eddy kinetic energy ($\overline{\text{EKE}}$);
 407 b) Time-series of the coherent eddy number and the average absolute coherent eddy amplitude;
 408 c) Map of the number of eddies; d) Map of the average absolute coherent eddy amplitude; Sea-
 409 sonal cycle of the e) number of eddies, f) positive coherent eddy amplitude, and g) negative
 410 coherent eddy amplitude. Different lines represent the same as in Figure 10.

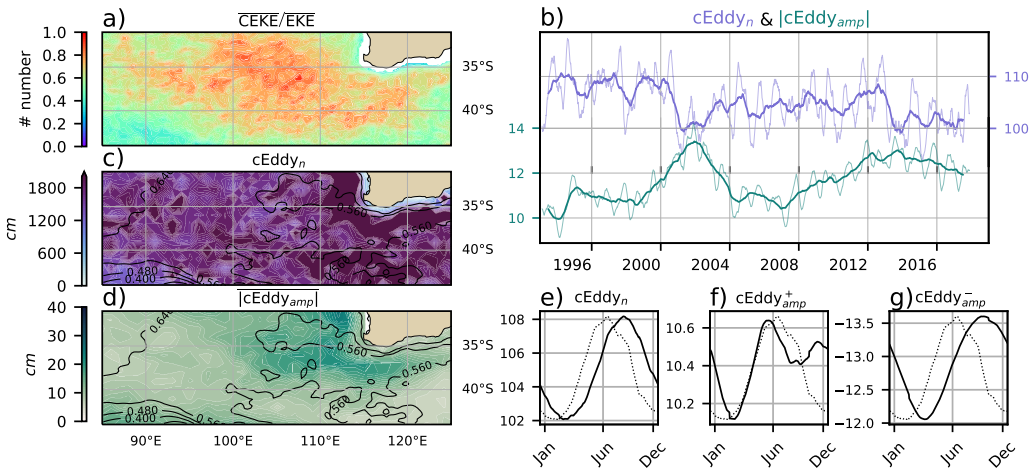
417 planation observed in Figure 6 of the lagged response of coherent eddy properties due
 418 to eddy-eddy interactions, consistent with the inverse cascade of energy.

425 Coherent eddies dominate the EKE field in other regions such as the Leeuwin Current
 426 (Figure 13), where the 65% of the energy is contained by coherent eddies. Although
 427 the Leeuwin region is not characterized by having a large EKE, however, a considerable
 428 abundance of eddies and large eddy amplitudes are observable in the region. The series
 429 reveal a significant increase in the $|\text{cEddy}_{amp}|$, while the cEddy_n has decreased over the
 430 last 3 decades (). The seasonal cycle shows that the cEddy_n peak occurs on August, 3
 431 months after the maximum winds (June). Meanwhile, the cEddy_{amp}^+ responds in syn-
 432 chrony to winds, and the cEddy_{amp}^- is in phase with the seasonal cycle of the cEddy_n .

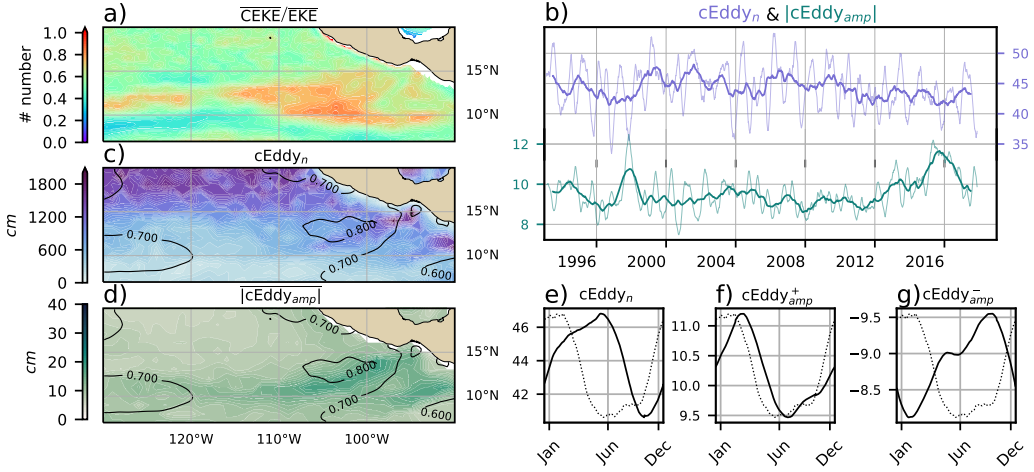
439 Another region with important contributions of the coherent eddy field is the East
 440 Tropical Pacific (Tehuantepec region; Figure 14), where coherent eddies contain ~58%
 441 of the energy. In fact, coherent eddy generation in this region is modulated by winds and
 442 coastally trapped waves which produce a strong horizontal and vertical shear (baroclinic



419 **Figure 12.** Climatology of the eddy field and coherent eddy field at the Agulhas Current. a)
 420 Ratio of mean coherent eddy kinetic energy ($\overline{\text{CEKE}}$) versus mean eddy kinetic energy ($\overline{\text{EKE}}$); b)
 421 Time-series of the coherent eddy number and the average absolute coherent eddy amplitude; c)
 422 Map of the number of eddies; d) Map of the average absolute coherent eddy amplitude; Seasonal
 423 cycle of the e) number of eddies, f) positive coherent eddy amplitude, and g) negative coherent
 424 eddy amplitude. Different lines represent the same as in Figure 10.



433 **Figure 13.** Climatology of the eddy field and coherent eddy field at the Leeuwin Current. a)
 434 Ratio of mean coherent eddy kinetic energy ($\overline{\text{CEKE}}$) versus mean eddy kinetic energy ($\overline{\text{EKE}}$); b)
 435 Time-series of the coherent eddy number and the average absolute coherent eddy amplitude; c)
 436 Map of the number of eddies; d) Map of the average absolute coherent eddy amplitude; Seasonal
 437 cycle of the e) number of eddies, f) positive coherent eddy amplitude, and g) negative coherent
 438 eddy amplitude. Different lines represent the same as in Figure 10.



452 **Figure 14.** Climatology of the eddy field and coherent eddy field at the East Tropical Pacific.
 453 a) Ratio of mean coherent eddy kinetic energy ($\overline{\text{CEKE}}$) versus mean eddy kinetic energy ($\overline{\text{EKE}}$);
 454 b) Time-series of the coherent eddy number and the average absolute coherent eddy amplitude;
 455 c) Map of the number of eddies; d) Map of the average absolute coherent eddy amplitude; Sea-
 456 sonal cycle of the e) number of eddies, f) positive coherent eddy amplitude, and g) negative
 457 coherent eddy amplitude. Different lines represent the same as in Figure 10.

443 and barotropic instabilities; Zamudio et al., 2006). Furthermore, the equatorial gener-
 444 ated waves propagating along the coast have an important interannual variability ob-
 445 servable in the $|\text{cEddy}_{\text{amp}}|$ time-series, where El Niño events are notable during 1997 and
 446 2015 (Figure 14b). The seasonal cycle of cEddy_n , $\text{cEddy}_{\text{amp}}^+$, and $\text{cEddy}_{\text{amp}}^-$ support the
 447 idea of a coherent eddies responding to two different coherent eddy generation mecha-
 448 nisms; the number of eddies seasonal cycle lags for by ~ 3 months from the winds, while
 449 the $\text{cEddy}_{\text{amp}}^+$ is on phase with the winds and the maximum of trapped waves (winter;
 450 Zamudio et al., 2006), and the $\text{cEddy}_{\text{amp}}^-$ could be a consequence of eddy-eddy interac-
 451 tions.

458 7 Discussion and Conclusions

459 We investigated the contribution of coherent eddies in the kinetic energy field us-
 460 ing satellite observations. We corroborate that around half of the EKE is explained by
 461 coherent eddies. This half is concentrated in eddy-rich regions where an intensification
 462 of the eddy field has been observed (Martínez-Moreno et al., 2021). The energy contained

463 by eddies is larger than the previous estimate of 40% by Chelton et al. (2011). Although
 464 there are difference in the identification criteria of both eddy identification methods, the
 465 main cause of the difference is believed to be the lifespan and amplitude filters. These
 466 filters are widely used to track individual eddies on space and time, however, interactions
 467 between eddies in energetic regions my obscure the abundance and influence of short-
 468 lived coherent eddies. Filters are not used in this study, and indeed a lack of filters could
 469 facilitates an under or over-estimation of the the energy contained by coherent eddies,
 470 when miss-identifying or miss-fitting a coherent eddy. Thus, the presented estimate rep-
 471 resents an upper limit of the energy contained by coherent eddies.

472 In addition, it should be noted that regions with first baroclinic Rossby radius of
 473 deformation smaller than 10km cannot be resolved by satellite observations. Thus, the
 474 energy contained by coherent eddies around latitudes of 60° and those near the shore
 475 are missed from this estimate, and remains unknown their role in the seasonal cycle and
 476 local dynamics. New satellite altimeter missions (SWOT) may allow to estimate energy
 477 contained by mesoscale coherent eddies outside the tropical region and the continental
 478 slope.

479 Hemispherical variability indicates a strong seasonal cycle of the EKE, CEKE, and
 480 eddy properties. The seasonal cycle of the CEKE in each hemisphere occurs as a con-
 481 sequence of numerous small coherent eddies interacting with each other (eddy-eddy in-
 482 teractions) and resulting in stronger, larger and more energetic coherent eddies during
 483 summer after a few months of the yearly coherent eddy number maxima. This results
 484 reveals eddy-eddy interactions and thus the transfer of energy from smaller coherent ed-
 485 dies to larger coherent eddies could explain the observed seasonal cycle of CEKE and
 486 coherent eddies properties.

487 Coherent eddy properties showcase a non-uniform long-term readjustment of the
 488 mesoscale eddy field. Overall, the eddy number has decreased globally at a significant
 489 rate of ~ 35 eddies per decade from ~ 4000 eddies identified globally on average each day.
 490 However, large proportions of the ocean show an strengthening of the mesoscale coher-
 491 ent eddy field at a rate greater than ~ 1 cm per decade. **Positive trends average 1cm**
 492 **per decade, negative trends average -0.7cm per decade. Global average 0.2cm**
 493 **per decade** This strengthening of the coherent eddy amplitude is attributed to an in-
 494 tensification of each coherent eddy polarity, rather than a readjustment of the coherent

495 eddy field to sea level rise. In other words, the coherent eddy amplitude intensification
496 is occurring in both coherent eddy polarities and explain a proportion of the previously
497 observed readjustments in the eddy field to long-term changes in the ocean forcing (Hu
498 et al., 2020; Wunsch, 2020; Martínez-Moreno et al., 2021). This long-term readjustment
499 showcases an intensification of the coherent eddy field, possibly due to long-term read-
500 justments in the ocean baroclinic and barotropic instabilities, as well as the strength of
501 the winds.

502 The reconstruction of the coherent eddies and their statistics have revealed regions
503 with important coherent eddy contributions and a distinct seasonal evolution of the co-
504 herent eddies. Remarkably, western boundary extensions generate eddies through the
505 instability of the main currents and the seasonal cycle of coherent eddies, CEKE, and
506 thus EKE could be associated with an inverse energy cascade observable through lagged
507 seasonal cycles in the coherent eddy statistics. In addition to this, the amplitude of the
508 seasonal cycle in the boundary extensions is two times larger than any other region, thus
509 the seasonality of the coherent eddies in boundary extensions dominate the hemispher-
510 ical seasonal cycle. Furthermore, the seasonal lag of the inverse energy cascade is cou-
511 pled with the presence of fronts, such is the case of western boundary extensions, and
512 our results are consistent with the notion of baroclinic instability generating eddies and
513 through eddy-eddy interactions an lagged inverse energy cascade.

514 The use of satellite observations in this study limit our ability to quantify the im-
515 portance of the inverse energy cascade seasonality in the control of the coherent eddy
516 seasonal cycle. As mentioned above, there is robust evidence of an increase in eddy-eddy
517 interactions, however we can not discard important contributions from other processes
518 such as the seasonal cycle of forcing and instabilities, which are crucial in the genera-
519 tion of coherent eddies. Although this study can provide a descriptive response of the
520 coherent eddy field, further studies are needed to asses the role of eddy-eddy interactions
521 in our changing climate, ocean dynamics, and biogeochemical process. Furthermore, the
522 SWOT mission could allow to advance our understanding of eddy-eddy interactions and
523 the seasonal cycle of scales smaller than mesoscale, which may provide further evidence
524 of the inverse energy cascade driving the coherent eddy seasonality.

525 **Acknowledgments**

526 Chelton & Schlax (2013) dataset was produced by SSALTO/DUACS and distributed by
 527 AVISO+ (<https://www.aviso.altimetry.fr/>) with support from CNES, developed
 528 and validated in collaboration with E.Mason at IMEDEA. Global coherent eddy recon-
 529 struction, coherent and non-coherent eddy kinetic energy datasets, in addition to grid-
 530 deded coherent eddy tracking datasets are publicly available at (<https://doi.org/10.5281/zenodo.4646429>). All analyses and figures in this manuscript are reproducible via Jupyter
 531 notebooks and instructions can be found in the Github repository CEKE_climatology
 532 (https://github.com/josuemtzmo/CEKE_climatology). Trends used the Python Pack-
 533 age xarrayMannKendall (<https://doi.org/10.5281/zenodo.4458776>)

534 **References**

- 535
- 536 Arbic, B. K., Polzin, K. L., Scott, R. B., Richman, J. G., & Shriver, J. F. (2013).
 537 On Eddy Viscosity, Energy Cascades, and the Horizontal Resolution of Gridded
 538 Satellite Altimeter Products*. *Journal of Physical Oceanography*, 43(2), 283–300.
 539 doi: 10.1175/jpo-d-11-0240.1
- 540 Ashkezari, M. D., Hill, C. N., Follett, C. N., Forget, G., & Follows, M. J. (2016).
 541 Oceanic eddy detection and lifetime forecast using machine learning methods.
 542 *Geophysical Research Letters*, 43(23). doi: 10.1002/2016gl071269
- 543 Beron-Vera, F. J., Wang, Y., Olascoaga, M. J., Goni, G. J., & Haller, G. (2013). Ob-
 544 jective Detection of Oceanic Eddies and the Agulhas Leakage. *Journal of Physical
 545 Oceanography*, 43(7), 1426–1438. doi: 10.1175/JPO-D-12-0171.1
- 546 Bouali, M., Sato, O. T., & Polito, P. S. (2017). Temporal trends in sea surface tem-
 547 perature gradients in the South Atlantic Ocean. *Remote Sensing of Environment*,
 548 194, 100–114. doi: 10.1016/j.rse.2017.03.008
- 549 Callies, J., Flierl, G., Ferrari, R., & Fox-Kemper, B. (2015). The role of mixed-layer
 550 instabilities in submesoscale turbulence. *Journal of Fluid Mechanics*, 788, 5–41.
 551 doi: 10.1017/jfm.2015.700
- 552 Cane, M. A., Clement, A. C., Kaplan, A., Kushnir, Y., Pozdnyakov, D., Seager, R.,
 553 ... Murtugudde, R. (1997). Twentieth-Century Sea Surface Temperature Trends.
 554 *Science*, 275(5302), 957–960. doi: 10.1126/science.275.5302.957
- 555 Chaudhuri, A. H., Gangopadhyay, A., & Bisagni, J. J. (2009). Interannual variabil-
 556 ity of Gulf Stream warm-core rings in response to the North Atlantic Oscillation.

- 557 *Continental Shelf Research*, 29(7), 856–869. doi: 10.1016/j.csr.2009.01.008
- 558 Chelton, D. B., A. d. R., Schlax, M. G., Naggar, K., & Siwetz, N. (1998). Geographical
559 variability of the first baroclinic Rossby radius of deformation. *Journal
560 of Physical Oceanography*, 28(3), 433-460. doi: 10.1175/1520-0485(1998)028<433:
561 GVOTFB>2.0.CO;2
- 562 Chelton, D. B., Gaube, P., Schlax, M. G., Early, J. J., & Samelson, R. M. (2011).
563 The influence of nonlinear mesoscale eddies on near-surface oceanic chlorophyll.
564 *Science*, 334(6054), 328-32. doi: 10.1126/science.1208897
- 565 Chelton, D. B., & Schlax, M. G. (2013). *Mesoscale eddies in altimeter observations
566 of ssh*.
- 567 Chelton, D. B., Schlax, M. G., Samelson, R. M., & de Szoeke, R. A. (2007). Global
568 observations of large oceanic eddies. *Geophysical Research Letters*, 34(15),
569 L15606. doi: 10.1029/2007GL030812
- 570 CMEMS. (2017). The Ssalto/Duacs altimeter products were produced and dis-
571 tributed by the Copernicus Marine and Environment Monitoring Service. *Aviso
572 Dataset*. Retrieved from <https://www.aviso.altimetry.fr/>
- 573 Cui, W., Wang, W., Zhang, J., & Yang, J. (2020). Identification and census statis-
574 tics of multicore eddies based on sea surface height data in global oceans. *Acta
575 Oceanologica Sinica*, 39(1), 41–51. doi: 10.1007/s13131-019-1519-y
- 576 Faghmous, J. H., Frenger, I., Yao, Y., Warmka, R., Lindell, A., & Kumar, V. (2015,
577 6). A daily global mesoscale ocean eddy dataset from satellite altimetry. *Scientific
578 Data*, 2, 150028 EP -. doi: 10.1038/sdata.2015.28
- 579 Ferrari, R., & Wunsch, C. (2009). Ocean Circulation Kinetic Energy: Reservoirs,
580 Sources, and Sinks. *Annual Review of Fluid Mechanics*, 41(1), 253–282. doi: 10
581 .1146/annurev.fluid.40.111406.102139
- 582 Frenger, I., Gruber, N., Knutti, R., & Münnich, M. (2013). Imprint of Southern
583 Ocean eddies on winds, clouds and rainfall. *Nature Geoscience*, 6(8), 608 EP -.
584 doi: 10.1038/ngeo1863
- 585 Frenger, I., Münnich, M., Gruber, N., & Knutti, R. (2015). Southern Ocean eddy
586 phenomenology. *Journal of Geophysical Research: Oceans*, 120(11), 7413-7449.
587 doi: 10.1002/2015JC011047
- 588 Fu, L., Chelton, D., Le Traon, P., & Oceanography, M. R. (2010). Eddy dynamics
589 from satellite altimetry. *Oceanography*, 23(4), 14-25. doi: 10.2307/24860859

- 590 Gill, A., Green, J., & Simmons, A. (1974). Energy partition in the large-scale ocean
591 circulation and the production of mid-ocean eddies. *Deep Sea Res Oceanogr Abstr*,
592 21(7), 499-528. doi: 10.1016/0011-7471(74)90010-2
- 593 Hogg, A. M., & Blundell, J. R. (2006). Interdecadal variability of the southern
594 ocean. *Journal of Physical Oceanography*, 36(8), 1626-1645. doi: 10.1175/
595 JPO2934.1
- 596 Hogg, A. M., Meredith, M. P., Chambers, D. P., Abrahamsen, E. P., Hughes,
597 C. W., & Morrison, A. K. (2015). Recent trends in the Southern Ocean
598 eddy field. *Journal of Geophysical Research: Oceans*, 120(1), 257-267. doi:
599 10.1002/2014JC010470
- 600 Hu, S., Sprintall, J., Guan, C., McPhaden, M. J., Wang, F., Hu, D., & Cai,
601 W. (2020, 2). Deep-reaching acceleration of global mean ocean circula-
602 tion over the past two decades. *Science Advances*, 6(6), eaax7727. doi:
603 10.1126/sciadv.aax7727
- 604 Japan Meteorological Agency, Japan. (2013). *Jra-55: Japanese 55-year reanalysis,*
605 *daily 3-hourly and 6-hourly data.* Boulder CO: Research Data Archive at the Na-
606 tional Center for Atmospheric Research, Computational and Information Systems
607 Laboratory. Retrieved from <https://doi.org/10.5065/D6HH6H41>
- 608 Kang, D., & Curchitser, E. N. (2013). Gulf stream eddy characteristics in a high-
609 resolution ocean model. *Journal of Geophysical Research: Oceans*, 118(9), 4474-
610 4487. Retrieved from <https://agupubs.onlinelibrary.wiley.com/doi/abs/10.1002/jgrc.20318> doi: <https://doi.org/10.1002/jgrc.20318>
- 612 Kang, D., & Curchitser, E. N. (2017). On the Evaluation of Seasonal Variability of
613 the Ocean Kinetic Energy. *Geophysical Research Letters*, 47, 1675-1583. doi: 10
614 .1175/JPO-D-17-0063.1
- 615 Li, G., Cheng, L., Zhu, J., Trenberth, K. E., Mann, M. E., & Abraham, J. P. (2020).
616 Increasing ocean stratification over the past half-century. *Nature Climate Change*,
617 1-8. doi: 10.1038/s41558-020-00918-2
- 618 Martínez-Moreno, J., Hogg, A. M., England, M., Constantinou, N. C., Kiss, A. E.,
619 & Morrison, A. K. (2021). Global changes in oceanic mesoscale currents over the
620 satellite altimetry record. *Journal of Advances in Modeling Earth Systems*, 0(ja).
621 doi: 10.1029/2019MS001769
- 622 Martínez-Moreno, J., Hogg, A. M., Kiss, A. E., Constantinou, N. C., & Morrison,

- 623 A. K. (2019). Kinetic energy of eddy-like features from sea surface altimetry. *Journal of Advances in Modeling Earth Systems*, 11(10), 3090-3105. doi: 10.1029/2019MS001769
- 624 Patel, R. S., Llort, J., Strutton, P. G., Phillips, H. E., Moreau, S., Pardo, P. C., & Lenton, A. (2020). The Biogeochemical Structure of Southern Ocean Mesoscale Eddies. *Journal of Geophysical Research: Oceans*, 125(8). doi: 10.1029/2020jc016115
- 625 Pilo, G. S., Mata, M. M., & Azevedo, J. L. L. (2015). Eddy surface properties and propagation at Southern Hemisphere western boundary current systems. *Ocean Science*, 11(4), 629–641. doi: 10.5194/os-11-629-2015
- 626 Qiu, B. (1999). Seasonal Eddy Field Modulation of the North Pacific Subtropical Counter-current: TOPEX/Poseidon Observations and Theory. *Journal of Physical Oceanography*, 29(10), 2471–2486. doi: 10.1175/1520-0485(1999)029<2471:sefmot>2.0.co;2
- 627 Qiu, B., & Chen, S. (2004). Seasonal Modulations in the Eddy Field of the South Pacific Ocean. *Journal of Physical Oceanography*, 34(7), 1515–1527. doi: 10.1175/1520-0485(2004)034<1515:smitef>2.0.co;2
- 628 Qiu, B., Chen, S., Klein, P., Sasaki, H., & Sasai, Y. (2014). Seasonal Mesoscale and Submesoscale Eddy Variability along the North Pacific Subtropical Counter-current. *Journal of Physical Oceanography*, 44(12), 3079–3098. doi: 10.1175/JPO-D-14-0071.1
- 629 Ruela, R., Sousa, M. C., deCastro, M., & Dias, J. M. (2020). Global and regional evolution of sea surface temperature under climate change. *Global and Planetary Change*, 190, 103190. doi: 10.1016/j.gloplacha.2020.103190
- 630 Sasaki, H., Klein, P., Qiu, B., & Sasai, Y. (2014). Impact of oceanic-scale interactions on the seasonal modulation of ocean dynamics by the atmosphere. *Nature Communications*, 5(1), 5636. doi: 10.1038/ncomms6636
- 631 Schubert, R., Schwarzkopf, F. U., Baschek, B., & Biastoch, A. (2019). Submesoscale Impacts on Mesoscale Agulhas Dynamics. *Journal of Advances in Modeling Earth Systems*, 11(8), 2745–2767. doi: 10.1029/2019ms001724
- 632 Siegel, D., Peterson, P., DJ, M., Maritorena, S., & Nelson, N. (2011). Bio-optical footprints created by mesoscale eddies in the Sargasso Sea. *Geophysical Research Letters*, 38(13), n/a-n/a. doi: 10.1029/2011GL047660

- 656 Uchida, T., Abernathey, R., & Smith, S. (2017). Seasonality of eddy kinetic energy
657 in an eddy permitting global climate model. *Ocean Modelling*, 118, 41–58. doi: 10
658 .1016/j.ocemod.2017.08.006
- 659 Wunsch, C. (2020). Is The Ocean Speeding Up? Ocean Surface Energy Trends.
660 *Journal of Physical Oceanography*, 50(11), 1–45. doi: 10.1175/jpo-d-20-0082.1
- 661 Wunsch, C., & Ferrari, R. (2004). Vertical mixing, energy, and the general circulation
662 of the oceans. *Annual Review of Fluid Mechanics*, 36(1), 281–314. doi: 10
663 .1146/annurev.fluid.36.050802.122121
- 664 Wyrtki, K., Magaard, L., & Hager, J. (1976). Eddy energy in the oceans. *Journal of*
665 *Geophysical Research*, 81(15), 2641–2646. doi: 10.1029/JC081i015p02641
- 666 Yue, S., & Wang, C. (2004). The Mann-Kendall Test Modified by Effective Sample
667 Size to Detect Trend in Serially Correlated Hydrological Series. *Water Resources*
668 *Management*, 18(3), 201–218. doi: 10.1023/b:warm.0000043140.61082.60
- 669 Zamudio, L., Hurlburt, H. E., Metzger, E. J., Morey, S. L., O'Brien, J. J., Tilburg,
670 C., & Zavala-Hidalgo, J. (2006). Interannual variability of Tehuantepec ed-
671 dies. *Journal of Geophysical Research: Oceans (1978–2012)*, 111(C5). doi:
672 10.1029/2005JC003182